nature physics

Article

https://doi.org/10.1038/s41567-022-01907-2

Antiferromagnetic metal phase in an electron-doped rare-earth nickelate

Received: 10 November 2021

Accepted: 2 December 2022

Published online: 30 January 2023

Check for updates

Qi Song[1,17], Spencer Doyle[1,17], Grace A. Pan[1], Ismail El Baggari[2], Dan Ferenc Segedin[1], Denisse Córdova Carrizales[1], Johanna Nordlander[1], Christian Tzschaschel[3], James R. Ehrets[1], Zubia Hasan[1], Hesham El-Sherif[2], Jyoti Krishna[4], Chase Hanson[4], Harrison LaBollita[4], Aaron Bostwick[5], Chris Jozwiak[5], Eli Rotenberg[5], Su-Yang Xu[3], Alessandra Lanzara[6,7], Alpha T. N'Diaye[5], Colin A. Heikes[8,9], Yaohua Liu[10,11], Hanjong Paik[12,13,14], Charles M. Brooks[1], Betül Pamuk[12], John T. Heron[15], Padraic Shafer[5], William D. Ratcliff[8,16], Antia S. Botana[4], Luca Moreschini[6,7,12] ✉ & Julia A. Mundy[1] ✉

Long viewed as passive elements, antiferromagnetic materials have emerged as promising candidates for spintronic devices due to their insensitivity to external fields and potential for high-speed switching. Recent work exploiting spin and orbital effects has identified ways to electrically control and probe the spins in metallic antiferromagnets, especially in non-collinear or non-centrosymmetric spin structures. The rare-earth nickelate $NdNiO_3$ is known to be a non-collinear antiferromagnet in which the onset of antiferromagnetic ordering is concomitant with a transition to an insulating state. Here we find that for low electron doping, the magnetic order on the nickel site is preserved, whereas electronically, a new metallic phase is induced. We show that this metallic phase has a Fermi surface that is mostly gapped by an electronic reconstruction driven by bond disproportionation. Furthermore, we demonstrate the ability to write to and read from the spin structure via a large zero-field planar Hall effect. Our results expand the already rich phase diagram of rare-earth nickelates and may enable spintronics applications in this family of correlated oxides.

In recent years, antiferromagnetic materials have become leading contenders for spintronic devices. Compared with their ferromagnetic counterparts, more subtle methods to control the ordered spins (writing) and to probe such control (reading) are required[1]. The most widely used method in antiferromagnets is the same as that in ferromagnets—measuring a component of the anisotropic magnetoresistance (AMR) signal[2,3]. This signal strength is typically limited to just a couple of per cents of the sample's resistance, thus limiting high-density applications[4]. This has driven parallel attempts to discover additional readout methods as well as to identify metallic antiferromagnets with larger AMR signals[5,6].

Here we develop a metallic antiferromagnet and demonstrate nearly an order of magnitude stronger AMR signal over conventional antiferromagnets. We begin with rare-earth nickelates ($RNiO_3$), transition metal oxides that sit at the boundary between localized and itinerant electron behaviours. With the exception of $LaNiO_3$, an unconventional metal[7] with the largest rare-earth cation R, $RNiO_3$ compounds undergo a metal–insulator transition (MIT) and a transition from a paramagnetic to a non-collinear antiferromagnetic state[8–10]. In $PrNiO_3$ and $NdNiO_3$ bulk crystals, the onsets of antiferromagnetic and insulating states are coincident ($T_{MIT} = T_N$)[10–13]. In addition, at the MIT, a breathing-mode distortion occurs where half of the NiO_6 octahedra are

A full list of affiliations appears at the end of the paper. ✉e-mail: lmoreschini@berkeley.edu; mundy@fas.harvard.edu

https://doi.org/10.1038/s41567-022-01907-2

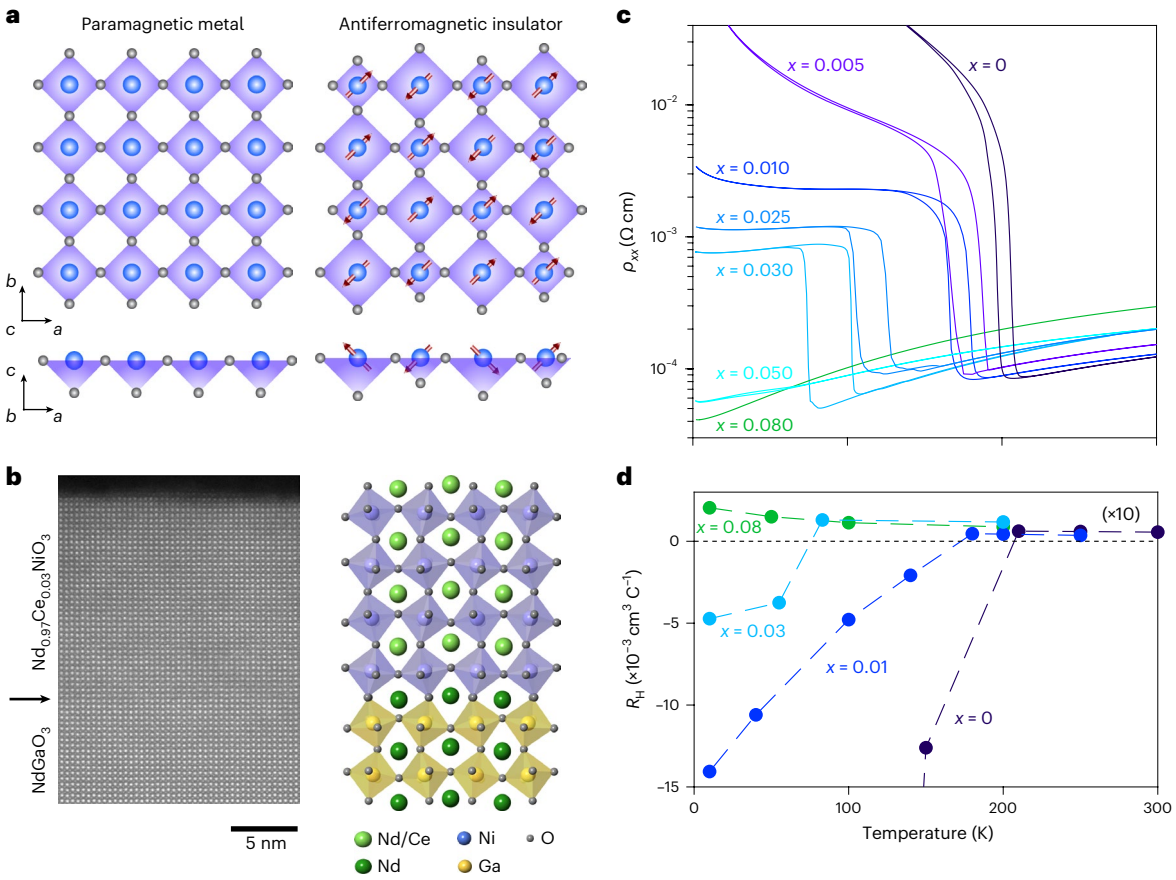

Fig. 1 | Structural and electrical characterization of $Ce_xNd_{1-x}NiO_3$ thin films. **a**, Crystal structure of $NdNiO_3$ viewed in the a–b and a–c plane. The simplified $(\frac{1}{2}, \frac{1}{2}, \frac{1}{2})$bond disproportionation and $(\frac{1}{4}, \frac{1}{4}, \frac{1}{4})$non-collinear antiferromagnetic order below T_{MIT} are illustrated on the right side. **b**, HAADF-STEM image of a $Ce_{0.03}Nd_{0.97}NiO_3$ film. The black arrow denotes the coherent substrate/film interface. **c**, Resistivity ρ versus temperature for $Ce_xNd_{1-x}NiO_3$ films synthesized on $NdGaO_3$. **d**, Hall coefficient R_H versus temperature for the same films, showing a change in sign lowering the temperature across T_{MIT} and T_{MMT}. The positive axis is scaled by a factor of 10 for visibility.

expanded and half are compressed in an alternating pattern: a charge order sets in without any $3d^6/3d^8$ charge fluctuation on the nickel sites, known as bond disproportionation[14–16] (Fig. 1a) (as is common practice, here we will interchangeably refer to this as bond disproportionation/ordering or charge ordering, implying that its origin is the hybridization between O 2*p* and Ni 3*d* states).

Although rare-earth nickelates display coupled spin, charge and lattice degrees of freedom, as well as robust metallic and antiferromagnetic states, to date, to the best of our knowledge, an antiferromagnetic metal phase has not yet been identified[17]. We choose $NdNiO_3$ which displays a direct transition from a paramagnetic metal to a non-collinear antiferromagnetic insulator at the highest temperature within the $RNiO_3$ series[18–20]. Previous studies have found that strong compressive strain[21–23] or hole doping on the neodymium site[24–26] tends to suppress the MIT and leaves a paramagnetic metal state, reminiscent of that found in $LaNiO_3$. In contrast, the electron doping of bulk crystals through Th^{4+} (ref. [25]) or Ce^{4+} (refs. [24,26]) substitution in place of Nd^{3+} has been reported to result only in a modest suppression of the MIT transition temperature. Other studies have found that electron doping through oxygen vacancies stabilizes a persistent antiferromagnetic state, yet this state is even more resistive than the parent $NdNiO_3$ phase[27,28].

Here we employ the electron doping of epitaxial $NdNiO_3$ thin films through the substitution of Ce^{4+} on the Nd^{3+} lattice site. We find that cerium substitution rapidly induces a metal–metal transition (MMT) where the low-temperature metallic phase retains the antiferromagnetism on the nickel sites of the parent $NdNiO_3$. In contrast to the metallic phase above the MMT and MIT, the Fermi surface below the MMT is largely gapped with spectral weight confined to discrete high-intensity spots. Moreover, in this low-temperature phase, we demonstrate heat-assisted magnetic recording with the maximum measured amplitude of 18%, bringing a family of materials into the spintronics community and suggesting a pathway to stronger AMR readout signals in antiferromagnets.

Epitaxial films of $Ce_xNd_{1-x}NiO_3$ were synthesized by reactive-oxide molecular-beam epitaxy on $(100)_{pc}$ $NdGaO_3$ ((110) in orthorhombic notation for the *Pnma* space group), which provides 1% tensile strain (Methods). All the crystallographic directions referenced throughout this work follow the pseudocubic (pc) notation. Figure 1b shows the high-angle annular dark-field scanning transmission electron microscopy (HAADF-STEM) image of the $Ce_{0.03}Nd_{0.97}NiO_3$ compound. Additional HAADF-STEM and electron energy-loss spectroscopy (EELS) maps found in the Supplementary Information support the high structural quality and absence of cerium phase segregation or local lattice deformations in these samples (Supplementary Figs. 1 and 5). X-ray absorption spectroscopy data on the Ce-$M_{4,5}$, Nd-$M_{4,5}$ and O-*K* pre-peak edges confirm the prototypical Ce^{4+} and Nd^{3+} valence states, and indicate electron doping onto the nickel sites (Supplementary Fig. 6).

As shown in Fig. 1c, cerium substitution results in qualitative changes in the transport properties of the films. The parent compound $NdNiO_3$ shows an MIT at ~200 K with a resistivity increase of about five orders of magnitude[29]. For intermediate cerium doping ($0.01 \leq$

https://doi.org/10.1038/s41567-022-01907-2

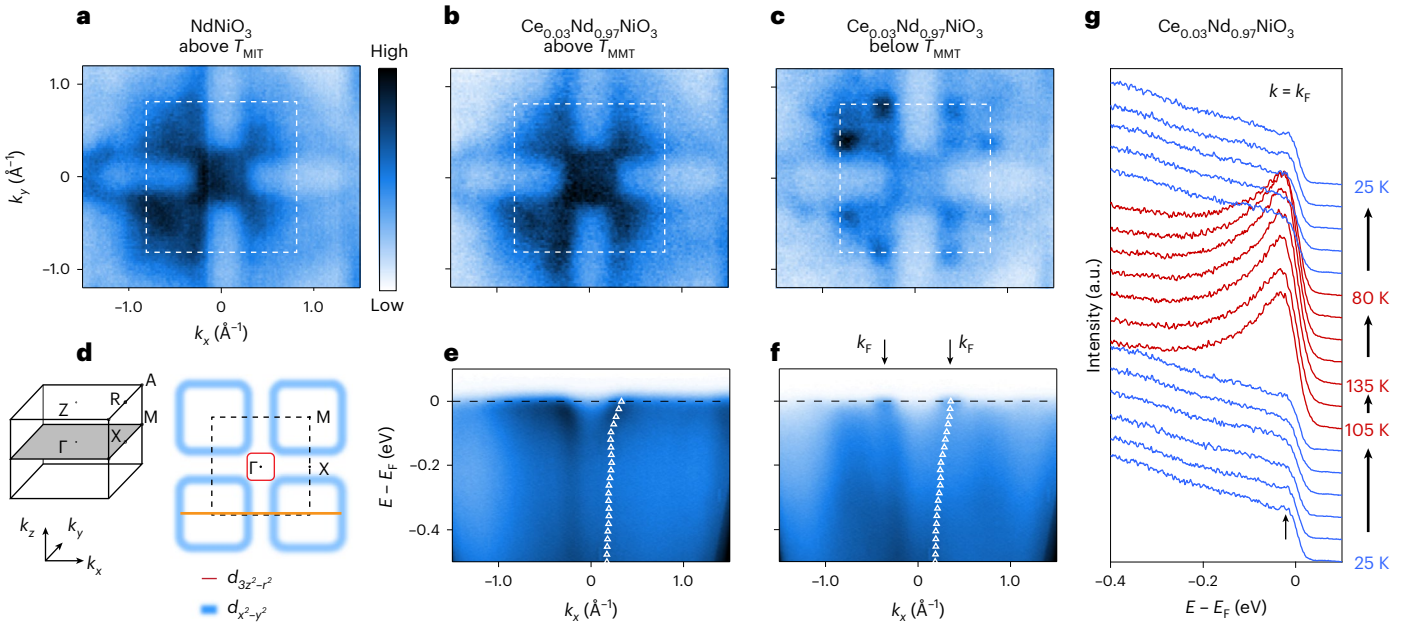

Fig. 2 | Electronic transition in $Ce_xNd_{1-x}NiO_3$ viewed by ARPES. a,**b**, Fermi surfaces of $NdNiO_3$ (**a**) and $Ce_{0.03}Nd_{0.97}NiO_3$ (**b**) measured at 200 K with $h\nu = 156$ eV corresponding to Γ_{004}. This is above the MIT for $NdNiO_3$ and MMT for $Ce_{0.03}Nd_{0.97}NiO_3$. The photoemission intensity is coded by the colour bar. **c**, Same data as in **b**, but measured at 25 K (below the MMT). **d**, Sketch of the $NdNiO_3$ three-dimensional Brillouin zone, using labels for the tetragonal geometry and Fermi surface on the Γ–X–M plane (for $NdNiO_3$, $\overline{\Gamma X} \simeq 0.81$ Å^{-1}). The $d_{x^2-y^2}$ contour is blurred to indicate that it is only visible in this plane due to the k_z broadening in the measurement. The horizontal line marks the M–X–M cuts (shown in **e** and **f**, and corresponding to the maps in **b** and **c**, respectively); the markers on the right indicate the peak positions extracted from the momentum distribution curves at intervals of 20 meV. The arrows in **f** point to the Fermi vector k_F. **g**, Energy distribution curves measured at k_F of $Ce_{0.03}Nd_{0.97}NiO_3$, cycling T from ~25 K (bottom) to ~130 K and then cooling back to ~25 K (top). The blue/red curves are measured below/above T_{MMT}, and the arrow indicates the quasiparticle peak at low temperature.

$x < 0.06$), the resistivity increases when cooling through the MMT but recovers a $d\rho/dT > 0$ behaviour, indicative of a metallic phase and an MMT as opposed to the MIT of the parent compound. These samples also demonstrate slight resistive upturns at a sufficiently low temperature (below about 10 K), but we believe this to be due to weak localization effects, as suggested by the negative magnetoresistance shown in Supplementary Fig. 21. For higher doping ($x > 0.06$), the transition is fully suppressed and the films remain metallic at all temperatures. We note that the emergence of this MMT transition and fully metallic samples were not observed in previous cerium-doped $NdNiO_3$ powder samples[24,26]. Our density functional theory (DFT) calculations (Supplementary Fig. 13) independently demonstrate this behaviour, too. In $NdNiO_3$, the sign of the Hall coefficient R_H (Fig. 1d) changes from positive to negative as the system is cooled below T_{MIT} (refs. [23,30]). The same sign change is observed for $0.01 \leq x < 0.06$ at T_{MMT}, indicating that a change in dominant charge carriers from holes to electrons still occurs across the MMT.

We use angle-resolved photoemission spectroscopy (ARPES) to show that the MMT results in a distinct fermiology at low temperatures. Figure 2a–c shows the ARPES data measured on the Γ–X–M high-symmetry plane of the three-dimensional Brillouin zone (Fig. 2d). The Fermi surface of $NdNiO_3$ above T_{MIT} consists of a small electron pocket centred at Γ (predominantly of the d_{z^2} orbital character) and a larger hole pocket centred at M (predominately of the $d_{x^2-y^2}$ character), visible due to k_z broadening intrinsic to the measurement. This band structure is consistent with prior measurements of $NdNiO_3$ above T_{MIT} (ref. [31]) and is equivalent to that of the fully metallic $LaNiO_3$ (refs. [32,33]). As shown in Fig. 2b, there are no perceptible differences between the Fermi surfaces of $Ce_{0.03}Nd_{0.97}NiO_3$ and $NdNiO_3$ at 200 K within the experimental resolution and data quality. In contrast, below T_{MMT}, the Fermi surface of $Ce_{0.03}Nd_{0.97}NiO_3$ does not vanish (Fig. 2c) as for insulating $NdNiO_3$ (ref. [31]) (Supplementary Fig. 7), but instead turns into a distinctive pattern of discontinuous high-intensity spots located roughly along the original hole pocket contour measured above the transition. This strong reduction in the spectral weight of the hole-like Fermi surface is consistent with the change in sign, from positive to negative, observed in R_H at T_{MMT} (Fig. 1d). For fully metallic $Ce_{0.1}Nd_{0.9}NiO_3$, the band structure does not show any temperature variation or any noticeable difference with respect to the metallic phase of $NdNiO_3$ (Supplementary Fig. 11). The existence of a unique low-temperature Fermi surface in the Ce-doped samples hosting an MMT helps to dismiss concerns of phase coexistence observed in prior nickelate research[29,34].

In Fig. 2e,f, we compare the dispersion above and below T_{MMT} for $Ce_{0.03}Nd_{0.97}NiO_3$ along the M–X–M line that cuts through one of the high-intensity spots. At high temperatures, the band shows a metallic Fermi edge over a broad momentum range, consistent with the Γ–X–M plane being close to the boundary of the hole pocket in the k_z direction. At low temperatures, the spectral weight at the Fermi level (E_F) is suppressed for most of the range, but at some k_x values, the metallic edge persists (Supplementary Figs. 8 and 10 show a more detailed analysis). Varying the temperature within either metallic phase does not result in any appreciable modification to the maps shown in Fig. 2e,f, whereas a change is instead abrupt at the transition. Figure 2g shows the evolution of the energy dispersion curves taken at the Fermi vector (k_F) determined in Fig. 2f, as the temperature is cycled through the MMT. During the warm up, the intensity at E_F suddenly converts into a broad peak at ~105 K that remains unchanged until cooling down to ~80 K, in a hysteresis cycle that perfectly matches the one observed in the resistivity curves shown in Fig. 1c. Notice that the energy dispersion curves of these hot spots retain a metallic edge over the whole temperature range. At the lowest temperature (~25 K), there is a distinguishable peak–dip lineshape with a small quasiparticle, as opposed to the rest of the Fermi surface that is gapped or pseudogapped below T_{MMT}

https://doi.org/10.1038/s41567-022-01907-2

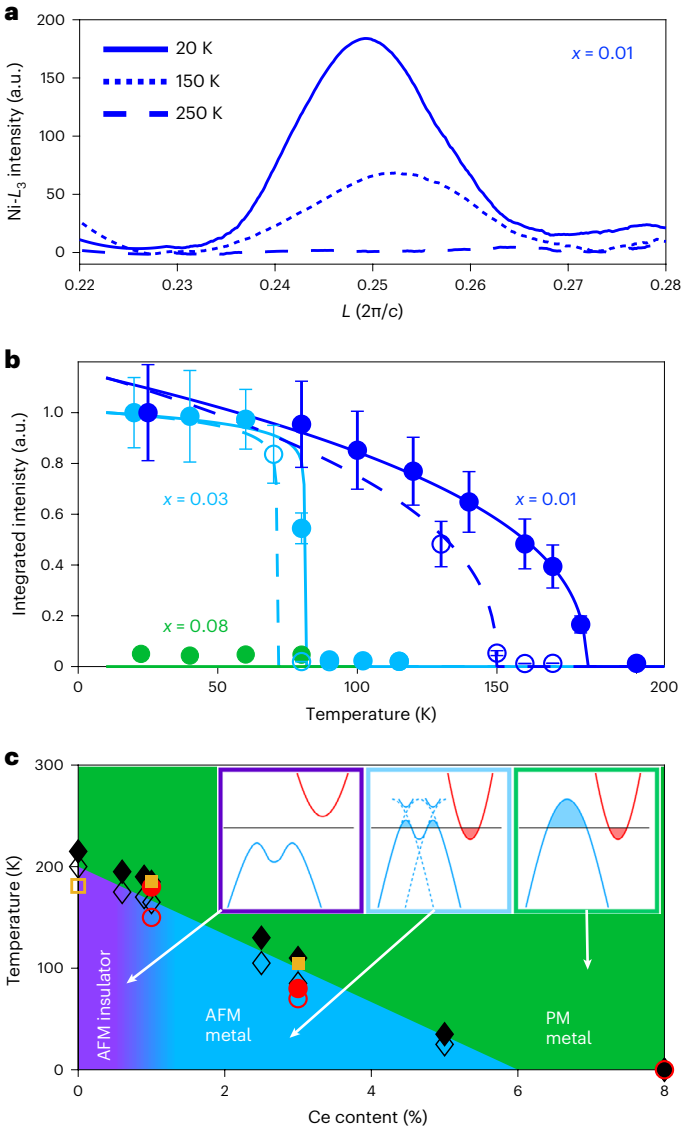

Fig. 3 | RXS data and phase diagram of $Ce_xNd_{1-x}NiO_3$. a, Ni-L_3-edge RXS scans along $L = q_z$ taken above and below T_{MMT} for a $Ce_{0.01}Nd_{0.99}NiO_3$ sample. We observe the onset of a $q = (\frac{1}{4}, \frac{1}{4}, \frac{1}{4})$ order below 200 K. **b**, Integrated intensity from the Ni-L_3-edge RXS data versus temperature for the $Ce_{0.01}Nd_{0.99}NiO_3$ and $Ce_{0.03}Nd_{0.99}NiO_3$ samples. The solid and dashed lines are guides to the eye for the warming and cooling data points, respectively. Data are presented as mean values ± standard error of the mean from the $n = 66$ or $n = 72$ pixels located in the region of interest around the scattering vector. **c**, Electronic and magnetic phase diagram extracted from this study on films synthesized on $NdGaO_3$ substrates. AFM and PM refer to antiferromagnetic and paramagnetic, respectively. The filled and empty symbols indicate the temperatures extracted for warming and cooling cycles, respectively, from electronic transport (◇), RXS (○) and ARPES (□) measurements. The insets show the schematic of the band structure for the three phases. The backfolding in the antiferromagnetic metallic phases is only shown for the hole pocket and without accounting for hybridization for simplicity.

(Supplementary Figs. 7–9). Thus, our electrical transport and ARPES measurements independently show the new metallic phase below the MMT in our intermediate cerium-doped samples.

The Fermi surface (Fig. 2c) clearly shows the presence of a new, smaller periodicity in momentum space. Even though it is difficult to sketch the band backfolding due to the presence of multiple bands and of the spectral weight added by k_z broadening, the pattern formed by the high-intensity spots is consistent with a $(\frac{1}{2}, \frac{1}{2}, \frac{1}{2})$ superstructure, where the Γ and A points are brought into each other, as well as Z and M (Supplementary Fig. 11). On the Z–R–A plane, weak signatures of this superstructure are present in (metallic) $LaNiO_3$ (ref. [32]), as well as here in $Ce_xNd_{1-x}NiO_3$ for all the doping levels above the MIT/MMT (Supplementary Fig. 11), which may originate from dynamic charge-order fluctuations (Supplementary Information)[15,35].

To probe the antiferromagnetic order in this low-temperature metallic phase, we use neutron diffraction and site-specific resonant X-ray scattering (RXS). Neutron diffraction (Supplementary Fig. 15) shows that the parent $NdNiO_3$ is antiferromagnetically ordered, as reported in the literature[9,36]. Figure 3a shows the RXS data from the Ni-L_3 edge of $Ce_{0.01}Nd_{0.99}NiO_3$, measured along l (q_z) with fixed $(h, k) = (\frac{1}{4}, \frac{1}{4})$. We observe an onset of $(\frac{1}{4}, \frac{1}{4}, \frac{1}{4})$ antiferromagnetic order below T_{MMT}. The temperature dependence of the (normalized) integrated signal is shown in Fig. 3b for $x = 0.01$, 0.03 and 0.08. The absolute integrated signal intensity decreases from the $x = 0.01$ to the $x = 0.03$ sample (Supplementary Fig. 15 and the accompanying discussion provide more details). As an additional verification of the antiferromagnetic order in the $x = 0.03$ sample, we performed optical second-harmonic generation measurements, which concur with the findings from the RXS measurements presented here (Supplementary Fig. 18). In contrast to $NdNiO_3$, the magnetic order on the neodymium sites is not present below T_{MMT}. This is apparent in the Nd-$M_{4,5}$ RXS as well as the absence of observed order in neutron scattering (which is primarily sensitive to the neodymium order) (Supplementary Fig. 15). Finally, the metallic $Ce_{0.08}Nd_{0.92}NiO_3$ film lacks observable magnetic ordering on either cation site. Note that we are unable to distinguish a collinear versus non-collinear microscopic ordering from the presented data; however, based on prior works, the non-collinear order is the most probable origin of the measured $(\frac{1}{4}, \frac{1}{4}, \frac{1}{4})$ periodicity in our samples[9,37].

The $Ce_xNd_{1-x}NiO_3$ system, thus, shows three distinct regions (Fig. 3c). For $x \lesssim 0.01$, there is a transition from a paramagnetic metal to an insulator with antiferromagnetic order on both neodymium and nickel sites. For $0.01 \lesssim x \lesssim 0.06$, the MIT is replaced by an MMT with antiferromagnetic order remaining on the nickel sites in the low-temperature metallic phase. For $x \gtrsim 0.06$, the material lacks evidence of magnetic order, and is probably a paramagnetic metal at all temperatures, similar to $LaNiO_3$ (ref. [38]) or $NdNiO_3$ under compressive strain[21–23].

Although the insulating phase in the $RNiO_3$ family is believed to result from a combination of lattice distortion and electronic correlations[14,15,39,40], the MMT offers the possibility to partially decouple two contributions to the transition: Peierls type and Mott type[41]. From our data shown in Fig. 2b,c, we argue that in this low-temperature metallic phase, the Peierls component of the MIT has taken place, but the additional electrons provided by the Ce^{4+} atoms probably screen correlations just enough that the electron and hole bands are not pushed apart. In this respect, note also that no sizeable bandwidth reduction is observed (Fig. 2e,f), where, both above and below T_{MMT}, the hole-like band disperses all the way to the onset of the t_{2g} manifold. In this scenario, the charge order is a necessary[42] but not sufficient condition to induce an insulating phase in the $RNiO_3$ family. With suppressed or reduced electronic correlations, the system remains metallic and retains the characteristic non-collinear antiferromagnetic order.

Finally, we demonstrate the manipulation of antiferromagnetic order in this newly stabilized antiferromagnetic metal phase with an external magnetic field, and probe the spin structure via electrical transport. We measure the zero-field planar Hall effect (ZF-PHE) of $Ce_{0.03}Nd_{0.97}NiO_3$ samples below T_{MMT}. Antiferromagnetic materials are expected to display an AMR signal in the presence of a magnetic field as the signal is even (not odd) with the local magnetic moments. Zero-field effects, however, are far less common in antiferromagnets and imply a change to the microscopic spin structure[43–45], typically

https://doi.org/10.1038/s41567-022-01907-2

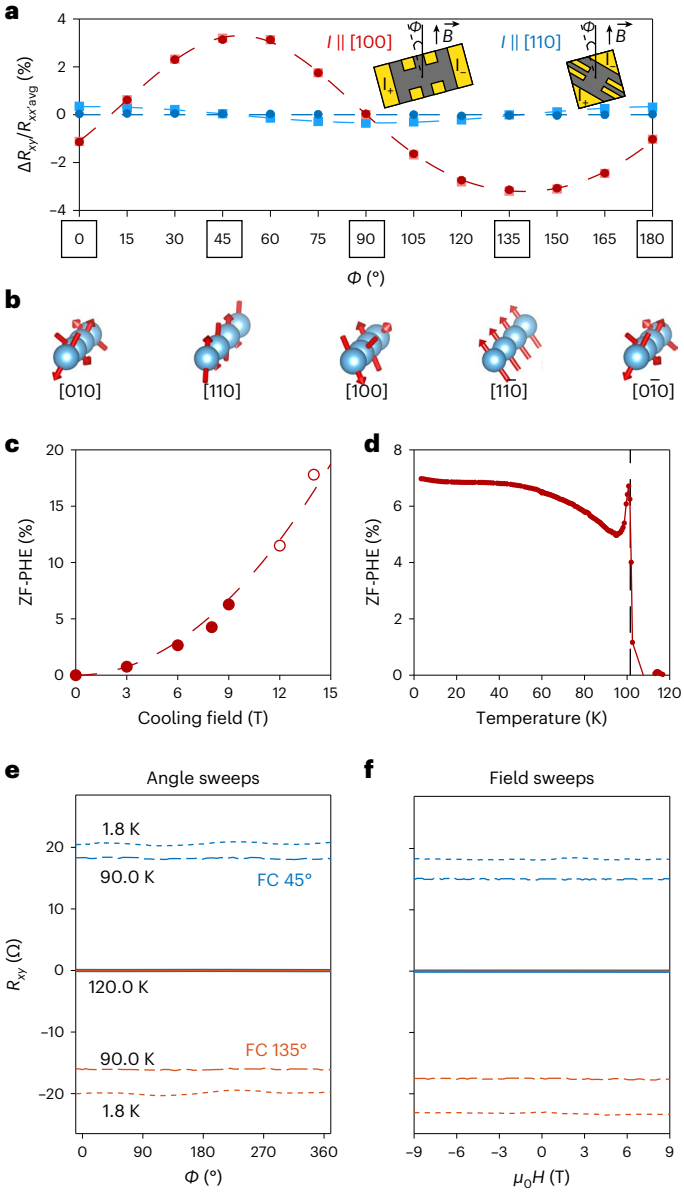

Fig. 4 | Large ZF-PHE in a metallic antiferromagnetic nickelate. a, Magnitude of PHE versus in-plane cooling field angle taken at 1.8 K for $I \parallel [100]$ (red) and $I \parallel [110]$ (blue). All data in this figure was taken on samples with $x = 0.02–0.03$. The light square points were taken with the field turned on (9 T), whereas the dark round points were taken after the removal of the field (0 T). The dashed lines serve as guides to the eye. The cartoon shows the sample geometry for $I \parallel [100]$. **b**, Views of the parent-compound spin structure for the $(\frac{1}{4}, \frac{1}{4}, \frac{1}{4})$ Néel vector viewed along different in-plane crystallographic directions corresponding to the (bold) in-plane rotation angles above. **c**,**d**, Dependence of ZF-PHE magnitude on the strength of the cooling field (**c**) and temperature (**d**) (9 T cooling field). High-field (12 and 14 T) scans were performed in an out-of-plane geometry (Supplementary Fig. 19). The dashed line in **c** is a quadratic fit to the data. **e**,**f**, Stability of the ZF-PHE resistance states to in-plane 9-T-field rotations (**e**) and ±9 T field sweeps (**f**). Rotations were performed after field cooling (FC) to 1.8 K to both maximum (45°; blue) and minimum (135°; orange) resistances. In field sweeps, the angle was changed to the opposite extreme after field cooling to 1.8 K (from 45° to 135° and vice versa) followed by a field sweep from +9 to −9 T.

preferential domain formation or canted moment orientation. Figure 4a shows the magnitude of the change in R_{xy} (normalized by the average R_{xx} value) versus in-plane angle ϕ for current (I) applied in two directions: parallel to [100] and parallel to [110]. When current is applied along [100], a substantial planar Hall effect (PHE) is present. As shown in Fig. 4a, removing the external magnetic field has minimal effect on the R_{xy} value, as the ZF-PHE (dark data points) is of the same magnitude as the 9 T PHE (light data points). There is, therefore, a memory effect written by a cooling field and read by the transverse resistance via the ZF-PHE. Conversely, for current parallel to [110], the 9 T PHE amplitude is reduced by almost an order of magnitude and with the removal of the field, entirely absent (Methods and Supplementary Fig. 19). Figure 4b shows a schematic of the spin structure of the parent compound $NdNiO_3$ (as found in previous works[20,37]) below the corresponding measurement angles (Fig. 4a). There is non-collinearity along [100] and [010], whereas along [110] and [$\bar{1}$10], the spins are collinear.

The amplitude of ZF-PHE for a given cooling field B_{FC} is defined as the overall difference between the peak (at 45°; Fig. 4a) and the trough (135°; Fig. 4a). We find the maximum amplitude of about 18%, which is roughly three times stronger than typically reported ZF-PHE magnitudes in antiferromagnets[4] and, to the best of our knowledge, almost equal to the maximum ever reported[45] (Supplementary Fig. 19). The dependence on B_{FC} (Fig. 4c) roughly follows a simple quadratic up to our maximum-used cooling field of 14 T, implying that with stronger fields, even larger amplitudes are attainable. The temperature dependence (Fig. 4d) shows a gradual weakening of the effect as the system approaches its transition and a sudden suppression above the MMT (consistent with the Néel transition). Figure 4e,f shows the constant-temperature angle and field sweeps taken after field cooling the sample at 45° (135°) into its 'high' ('low') R_{xy} state. The field-cooled states are extremely rigid to external perturbations once they are set; field sweeps over ±9 T and rotations in 9 T have a negligible impact on the R_{xy} channel. This is true at the lowest base temperature of 1.8 K as well as at temperatures near but below the transition (90.0 K; Fig. 4d).

In ferromagnets, there exist multiple contributions to the AMR signal arising from spin-dependent scattering between the conduction electrons and localized magnetic moments[46]. The degree of polarization of the conduction electrons critically affects the AMR amplitude. In collinear antiferromagnets, the current is strictly not spin polarized. But in non-collinear antiferromagnets, spin-polarized currents are generally allowed[47], and thus, the nature of how spin-dependent scattering events contribute to the AMR signal is changed. Given our current direction dependence, it is probable that a spin-polarized current in a non-collinear antiferromagnet either strengthens or allows additional scattering terms that, in turn, strengthen the ZF-PHE. Follow-up measurements in other non-collinear antiferromagnets would help clarify whether a large amplitude ZF-PHE is a general trend in such systems. Another natural follow-up experiment would be to attempt to electrically switch these devices using current pulses[48].

Here we explored the electron doping of a prototypical transition metal oxide, namely, $NdNiO_3$. The parent $NdNiO_3$ phase is characterized by both spin and charge ordering, perched at the boundary between localized and itinerant electron behaviours: a transition to an insulating, antiferromagnetic state happens in tandem with bond disproportionation. We showed that electron doping can uncover a metallic phase that preserves antiferromagnetic order on the nickel sites and is triggered by a Fermi-surface reconstruction induced by charge ordering. We interpret the new phase synthesized as one giving the opportunity of partially decoupling the lattice and electronic contributions to the famous MIT characteristic of perovskite nickelates. We also find that electron-doped samples display a large ZF-PHE and thus offer a new (possibly non-collinear) antiferromagnetic metal of relevance to the spintronics community.

Online content

Any methods, additional references, Nature Portfolio reporting summaries, source data, extended data, supplementary information, acknowledgements, peer review information; details of author contributions and competing interests; and statements of data and code availability are available at https://doi.org/10.1038/s41567-022-01907-2.

References

1. Baltz, V. et al. Antiferromagnetic spintronics. *Rev. Mod. Phys.* **90**, 015005 (2018).
2. McGuire, T. & Potter, R. Anisotropic magnetoresistance in ferromagnetic 3D alloys. *IEEE Trans. Magn.* **11**, 1018–1038 (1975).
3. Daughton, J. Magnetoresistive memory technology. *Thin Solid Films* **216**, 162–168 (1992).
4. Jungwirth, T., Marti, X., Wadley, P. & Wunderlich, J. Antiferromagnetic spintronics. *Nat. Nanotechnol.* **11**, 231–241 (2016).
5. Sürgers, C. et al. Switching of a large anomalous Hall effect between metamagnetic phases of a non-collinear antiferromagnet. *Sci. Rep.* **7**, 42982 (2017).
6. Arpaci, S. et al. Observation of current-induced switching in non-collinear antiferromagnetic $IrMn_3$ by differential voltage measurements. *Nat. Commun.* **12**, 3828 (2021).
7. Zhou, J., Marshall, L. & Goodenough, J. Mass enhancement versus Stoner enhancement in strongly correlated metallic perovskites: $LaNiO_3$ and $LaCuO_3$. *Phys. Rev. B* **89**, 245138 (2014).
8. Torrance, J., Lacorre, P., Nazzal, A., Ansaldo, E. & Niedermayer, C. Systematic study of insulator-metal transitions in perovskites $RNiO_3$ (R=Pr, Nd, Sm, Eu) due to closing of charge-transfer gap. *Phys. Rev. B* **45**, 8209–8212 (1992).
9. Scagnoli, V. et al. Role of magnetic and orbital ordering at the metal-insulator transition in $NdNiO_3$. *Phys. Rev. B* **73**, 100409 (2006).
10. Bodenthin, Y. et al. Magnetic and electronic properties of $RNiO_3$ (R=Pr, Nd, Eu, Ho and Y) perovskites studied by resonant soft X-ray magnetic powder diffraction. *J. Condens. Matter Phys.* **23**, 036002 (2011).
11. Medarde, M. Structural, magnetic and electronic properties of $RNiO_3$ perovskites (R=rare earth). *J. Phys.: Condens. Matter* **9**, 1679–1707 (1997).
12. Catalano, S. et al. Rare-earth nickelates $RNiO_3$: thin films and heterostructures. *Rep. Prog. Phys.* **81**, 046501 (2018).
13. Middey, S. et al. Physics of ultrathin films and heterostructures of rare-earth nickelates. *Annu. Rev. Mater. Res.* **46**, 305–334 (2016).
14. Johnston, S., Mukherjee, A., Elfimov, I., Berciu, M. & Sawatzky, G. Charge disproportionation without charge transfer in the rare-earth-element nickelates as a possible mechanism for the metal-insulator transition. *Phys. Rev. Lett.* **112**, 106404 (2014).
15. Green, R., Haverkort, M. & Sawatzky, G. Bond disproportionation and dynamical charge fluctuations in the perovskite rare-earth nickelates. *Phys. Rev. B* **94**, 195127 (2016).
16. Varignon, J., Grisolia, M., íñiguez, J., Barthélémy, A. & Bibes, M. Complete phase diagram of rare-earth nickelates from first-principles. *npj Quantum Mater.* **2**, 21 (2017).
17. Wang, B. et al. Antiferromagnetic defect structure in $LaNiO_{3-\delta}$ single crystals. *Phys. Rev. Mater.* **2**, 064404 (2018).
18. Lacorre, P. et al. Synthesis, crystal structure, and properties of metallic $PrNiO_3$: comparison with metallic $NdNiO_3$ and semiconducting $SmNiO_3$. *J. Solid State Chem.* **91**, 225–237 (1991).
19. García-Muñoz, J., Rodríguez-Carvajal, J., Lacorre, P. & Torrance, J. Neutron-diffraction study of $RNiO_3$ (R=La, Pr, Nd, Sm): electronically induced structural changes across the metal-insulator transition. *Phys. Rev. B* **46**, 4414–4425 (1992).
20. Frano, A. et al. Orbital control of noncollinear magnetic order in nickel oxide heterostructures. *Phys. Rev. Lett.* **111**, 106804 (2013).
21. Liu, J. et al. Strain-mediated metal-insulator transition in epitaxial ultrathin films of $NdNiO_3$. *Appl. Phys. Lett.* **96**, 1–4 (2010).
22. Mikheev, E. et al. Tuning bad metal and non-Fermi liquid behavior in a Mott material: rare-earth nickelate thin films. *Sci. Adv.* **1**, 21–26 (2015).
23. Hauser, A. et al. Correlation between stoichiometry, strain, and metal-insulator transitions of $NdNiO_3$ films. *Appl. Phys. Lett.* **106**, 092104 (2015).
24. Cheong, S., Hwang, H., Batlogg, B., Cooper, A. & Canfield, P. Electron-hole doping of the metal-insulator transition compound $RENiO_3$. *Phys. B: Condens. Matter* **194–196**, 1087–1088 (1994).
25. Alonso, J., Martínez-Lope, M. & Hidalgo, M. Hole and electron doping of $RNiO_3$ (R=La, Nd). *J. Solid State Chem.* **116**, 146–156 (1995).
26. García-Muñoz, J., Suaaidi, M., Martínez-Lope, M. & Alonso, J. Influence of carrier injection on the metal-insulator transition in electron- and hole-doped $R_{1-x}A_xNiO_3$ perovskites. *Phys. Rev. B* **52**, 13563–13569 (1995).
27. Li, J. et al. Sudden collapse of magnetic order in oxygen-deficient nickelate films. *Phys. Rev. Lett.* **126**, 187602 (2021).
28. Heo, S., Oh, C., Son, J. & Jang, H. Influence of tensile-strain-induced oxygen deficiency on metal-insulator transitions in $NdNiO_{3-\delta}$ epitaxial thin films. *Sci. Rep.* **7**, 4681 (2017).
29. Granados, X., Fontcuberta, J., Obradors, X., Mañosa, L. & Torrance, J. Metallic state and the metal-insulator transition of $NdNiO_3$. *Phys. Rev. B* **48**, 11666–11672 (1993).
30. Hauser, A. et al. Temperature-dependence of the Hall coefficient of $NdNiO_3$ thin films. *Appl. Phys. Lett.* **103**, 182105 (2013).
31. Dhaka, R. et al. Tuning the metal-insulator transition in $NdNiO_3$ heterostructures via Fermi surface instability and spin fluctuations. *Phys. Rev. B* **92**, 035127 (2015).
32. Yoo, H. et al. Latent instabilities in metallic $LaNiO_3$ films by strain control of Fermi-surface topology. *Sci. Rep.* **5**, 8746 (2015).
33. King, P. et al. Atomic-scale control of competing electronic phases in ultrathin $LaNiO_3$. *Nat. Nanotechnol.* **9**, 443–447 (2014).
34. Obradors, X. et al. Pressure dependence of the metal-insulator transition in the charge-transfer oxides $RNiO_3$ (R=Pr, Nd, $Nd_{0.7}La_{0.3}$). *Phys. Rev. B* **47**, 12353–12356 (1993).
35. Piamonteze, C. et al. Short-range charge order in $RNiO_3$ perovskites (R=Pr, Nd, Eu, Y) probed by X-ray-absorption spectroscopy. *Phys. Rev. B* **71**, 012104 (2005).
36. Scagnoli, V. et al. Induced noncollinear magnetic order of Nd^{3+} in $NdNiO_3$ observed by resonant soft X-ray diffraction. *Phys. Rev. B* **77**, 14–17 (2008).
37. Hepting, M. et al. Complex magnetic order in nickelate slabs. *Nat. Phys.* **14**, 1097–1102 (2018).
38. Sreedhar, K. et al. Electronic properties of the metallic perovskite $LaNiO_3$: correlated behavior of 3*d* electrons. *Phys. Rev. B* **46**, 6382–6386 (1992).
39. Mazin, I. et al. Charge ordering as alternative to Jahn-Teller distortion. *Phys. Rev. Lett.* **98**, 176406 (2007).
40. Georgescu, A., Peil, O., Disa, A., Georges, A. & Millis, A. Disentangling lattice and electronic contributions to the metal-insulator transition from bulk vs. layer confined $RNiO_3$. *Proc. Natl Acad. Sci. USA* **116**, 14434–14439 (2019).
41. Ruppen, J. et al. Optical spectroscopy and the nature of the insulating state of rare-earth nickelates. *Phys. Rev. B* **92**, 155145 (2015).
42. Zhang, J., Kim, H., Mikheev, E., Hauser, A. & Stemmer, S. Key role of lattice symmetry in the metal-insulator transition of $NdNiO_3$ films. *Sci. Rep.* **6**, 23652 (2016).
43. Marti, X. et al. Room-temperature antiferromagnetic memory resistor. *Nat. Mater.* **13**, 367–374 (2014).
44. Kriegner, D. et al. Multiple-stable anisotropic magnetoresistance memory in antiferromagnetic MnTe. *Nat. Commum.* **7**, 11623 (2016).
45. Nair, N. et al. Electrical switching in a magnetically intercalated transition metal dichalcogenide. *Nat. Mater.* **19**, 153–157 (2020).
46. Kokado, S., Tsunoda, M., Harigaya, K. & Sakuma, A. Anisotropic magnetoresistance effects in Fe, Co, Ni, Fe_4N, and half-metallic ferromagnet: a systematic analysis. *J. Phys. Soc. Jpn* **81**, 024705 (2012).

47. Železný, J., Zhang, Y., Felser, C. & Yan, B. Spin-polarized current in noncollinear antiferromagnets. *Phys. Rev. Lett.* **119**, 187204 (2017).
48. Wadley, P. et al. Electrical switching of an antiferromagnet. *Science* **351**, 587–590 (2016).

[1]Department of Physics, Harvard University, Cambridge, MA, USA. [2]The Rowland Institute at Harvard, Harvard University, Cambridge, MA, USA. [3]Department of Chemistry and Chemical Biology, Harvard University, Cambridge, MA, USA. [4]Department of Physics, Arizona State University, Tempe, AZ, USA. [5]Advanced Light Source, Lawrence Berkeley National Laboratory, Berkeley, CA, USA. [6]Department of Physics, University of California at Berkeley, Berkeley, CA, USA. [7]Materials Sciences Division, Lawrence Berkeley National Laboratory, Berkeley, CA, USA. [8]NIST Center for Neutron Research, National Institute of Standards and Technology, Gaithersburg, MD, USA. [9]Joint Quantum Institute, National Institute of Standards and Technology and the University of Maryland, Gaithersburg, MD, USA. [10]Neutron Scattering Division, Oak Ridge National Lab, Oak Ridge, TN, USA. [11]Second Target Station, Oak Ridge National Laboratory, Oak Ridge, TN, USA. [12]Platform for the Accelerated Realization, Analysis and Discovery of Interface Materials (PARADIM), Cornell University, Ithaca, NY, USA. [13]School of Electrical and Computer Engineering, University of Oklahoma, Norman, OK, USA. [14]Center for Quantum Research and Technology (CQRT), University of Oklahoma, Norman, OK, USA. [15]Department of Materials Science and Engineering, University of Michigan, Ann Arbor, MI, USA. [16]Department of Materials Science and Engineering, University of Maryland, College Park, MD, USA. [17]These authors contributed equally: Qi Song, Spencer Doyle. ✉e-mail: lmoreschini@berkeley.edu; mundy@fas.harvard.edu

Methods

Growth of $Nd_{1-x}Ce_xNiO_3$ films

$Ce_xNd_{1-x}NiO_3$ thin films were synthesized on $NdGaO_3$(110) and $LaAlO_3$(100) substrates by reactive-oxide molecular-beam epitaxy in a Veeco GEN10 system at the PARADIM Thin Film Growth Facility at Cornell University. The substrates were heated to 650 °C, determined by a thermocouple next to the substrate heater. A mixture of 80% ozone and 20% oxygen (partial pressure, 2×10^{-6} torr) was used during deposition (1 torr = 0.133322 kPa). Neodymium, cerium and nickel were evaporated from elemental sources. The fluxes of neodymium and nickel were 1×10^{13} atoms cm^2 s^{-1} and the flux of cerium was adjusted according to the desired doping. Following calibration using a quartz crystal microbalance, the three fluxes were first refined by measuring the thickness of Nd_2O_3 on the $(ZrO_2)_{0.905}(Y_2O_3)_{0.09}$(111) substrate (denoted as YSZ), CeO_2 on YSZ(111) substrate and NiO on MgO(100) substrate. The neodymium and nickel fluxes were then adjusted to produce a stoichiometric $NdNiO_3$ film as judged by the out-of-plane lattice parameter measured by X-ray diffraction and resistivity. The thickness of the deposited films varies between 14 and 23 nm. The structure was characterized by a PANalytical Empyrean X-ray diffractometer at 45 kV and 40 mA with Cu $K\alpha_1$ radiation. The X-ray diffraction θ–2θ scans indicate that all the $Ce_xNd_{1-x}NiO_3$ films are single phase and grown on $NdGaO_3$ (Supplementary Fig. 2) and $LaAlO_3$ (Supplementary Fig. 3) substrates. A comparison of the phase diagrams of the films grown on $NdGaO_3$ and $LaAlO_3$ is shown in Supplementary Fig. 4.

Resonant x-ray scattering

RXS measurements were performed on Ni-L_3 and Nd-M_5 edges at Beamline 4.0.2 at the Advanced Light Source, Lawrence Berkeley National Laboratory. Reciprocal space maps were generated by aligning to the signal peak after performing L-rod scans, and capturing fixed-geometry charge-coupled device images for bins around the peak location. Note that the deviation in peak maximum from the expected $L = 0.25$ is small enough to be due to an alignment offset, and is not directly indicative of any incommensurate order. Reciprocal space maps were measured at a series of temperatures on warming and cooling each sample, and regions of interest were defined around the observed order peaks. To extract the integrated intensities, constant-size regions of interest were defined around the peak in the reciprocal space maps, and the total intensity contained was summed. Background intensities (used for background subtraction) were collected in the diffuse regions around the ordering peaks. Small Q_x and Q_y offsets were added relative to the location of the $(\frac{1}{4}, \frac{1}{4}, \frac{1}{4})$ peak to define a region of background intensity.

X-ray absorption spectroscopy

We use Beamlines 6.3.1 and 4.0.2 at the Advanced Light Source, Lawrence Berkeley National Laboratory, to perform X-ray absorption spectroscopy. The measurements were conducted in the total electron yield geometry. Each spectrum shown is an average of 4–16 individual scans. The Nd-$M_{4,5}$ and Ce-$M_{4,5}$ spectra were normalized to the pre-edge intensity. The O-K edge spectra were normalized to the integrated peak intensity.

Transport measurements

Here Cr(10 nm)/Au(100 nm) electrical contacts were deposited in the pattern shown in Fig. 4a with an electron-beam evaporator. The channels were etched with a diamond scribe. A typical device was roughly 3 mm × 5 mm. Transport measurements were performed in a Quantum Design Dynacool physical property measurement system for fields up to 9 T. In-plane rotations were performed using the Quantum Design horizontal rotator option. Measurements performed at 12 and 14 T were conducted in a 14 T Quantum Design physical property measurement system. Hall coefficients were calculated from linear fits of antisymmetrized field sweeps measured from ±9 T; a representative example is shown in Supplementary Fig. 22. In Fig. 4e,f, a vertical offset due to contact misalignment was removed.

Angle-resolved photoemission spectroscopy

The ARPES data were measured at the MAESTRO beamline of the Advanced Light Source using a Scienta 4000 electron analyser. The angular resolution is better than 0.1° and the energy resolution varied between 10 and 25 meV depending on the chosen setting. Light polarization was set to p. In this configuration, when the sample is facing the analyser slit with the a axis in the horizontal (x) direction, the electric field is even in the x–z mirror plane plane containing the surface normal, and therefore, the measurement is sensitive to the $d_{x^2-y^2}$ and d_{z^2} orbitals along k_x, which are both even in the same plane. Before the ARPES experiments, the films were annealed in a partial oxygen pressure of 1×10^{-5} with ~10% ozone at a temperature of 420 °C for approximately 1 h.

Neutron scattering measurements

Elastic neutron scattering data were collected at the SPINS cold-neutron triple-axis spectrometer at the NIST Center for Neutron Research (NCNR) and the CORELLI elastic diffuse scattering spectrometer[49] at the Oak Ridge National Laboratory Spallation Neutron Source. The SPINS measurements were taken at a fixed neutron energy of 5 meV with a collimation and filter setup of 80′-Be-80′-Be using a standard closed-cycle refrigerator for sample temperature control.

CORELLI is a quasi-Laue time-of-flight instrument with an incident neutron wavelength band between 0.65 and 2.90 Å. The two-dimensional detector array of CORELLI spans from −19° to 147° in the horizontal plane and from −27° to 29° vertically. Therefore, a large three-dimensional volumetric reciprocal space is surveyed for a single sample orientation. The sample was mounted on an Al pin at the bottom of a close-cycle refrigerator, which provided a base temperature of 3 K at NCNR and 6 K at CORELLI. The sample was mounted with the $(hk0)_o$ plane horizontal and the vertical rotation axis was along the $(00l)_o$ axis. The experiments were conducted by first rotating the film through 120° in 1° step to survey the features in the large reciprocal space; then, the data were collected for an extended time with particular sample orientations optimized for the selected reciprocal regions.

High-angle annular dark-field scanning transmission electron microscopy

HAADF-STEM measurements were performed either on a JEOL ARM 200F (on the Ce 4% sample) or a Thermo Fisher Scientific Titan Themis Z G3 (on the Ce 12% sample), both operating at 200 kV. The convergence angle was either 19.6 or 22.0 mrad and the collection angle ranged from 68 to 280 mrad. Fast-acquisition frames were collected, aligned and summed to minimize the drift and obtain a high signal-to-noise ratio. The interfacial strain maps were extracted using the method described in another work[50].

Electron energy loss spectroscopy

The EELS measurements were performed on a Thermo Fisher Scientific Titan Themis Z G3 equipped with a Gatan Continuum spectrometer and imaging filter. The microscope was operated at 200 kV and 100 pA current. Dual (zero-loss and core-loss) EELS spectrum images were simultaneously acquired to correct for energy drift. After determining a region of interest in a zone axis, the electron beam was blocked for 15 min to stabilize and minimize the stage drift. The total spectrum imaging time was maintained between 30 to 100 s to minimize stage drifting. EELS maps were acquired with a 6-Å-pixel-size sampling, a 30 ms pixel dwell time and 0.75 eV per channel electron dispersion.

To extract the elemental composition maps, the EELS spectra were background subtracted up to the relevant elemental edge and then integrated. The background was modelled as a linear combination of power laws and the background window was selected to be as wide

as possible to obtain good fits. The energy windows were as follows: Ni-$L_{2,3}$ edge (851–878 eV), Ce-$M_{4,5}$ edge (881–913 eV) and Nd-$M_{4,5}$ edge (975–1,010 eV).

Computational methods

DFT-based calculations were performed using the all-electron, full potential code WIEN2k based on the augmented plane wave plus local orbital basis set[51]. For the exchange–correlation functional, we have used the Perdew–Burke–Ernzerhof implementation of the generalized gradient approximation[52]. In spin-polarized calculations, to treat the correlated Ni*d* states, we added static mean-field correlations as implemented in the DFT + *U* framework[53] with an onsite Coulomb *U* repulsion ranging from 2 to 5 eV and a non-zero Hund's coupling $J = 0.7$ eV to account for the anisotropies of the interaction[54]. The results presented here are consistent for this range of *U* values.

Phonon calculations were performed using the Vienna ab initio software package[55,56], which implements the projector augmented-wave formalism of DFT with an interface to Phonopy[57] (version 2.9.1) for plotting the phonon dispersion. The same DFT + *U* framework as mentioned above was added to the generalized gradient approximation/Perdew–Burke–Ernzerhof functionals. We employed an electronic energy tolerance of 10^{-8} eV and a force tolerance of 10^{-3} eV Å^{-1} for structural relaxations, with a Gaussian smearing of 0.005 eV, and an electronic-momentum *k*-point mesh of $2 \times 2 \times 2$ for a $4 \times 4 \times 4$ supercell structure. We obtain similar phonon instabilities with an electronic-momentum *k*-point mesh of $5 \times 5 \times 5$ for a $2 \times 2 \times 2$ supercell structure.

Data availability

The data presented in the figures and other findings of this study are available from the corresponding authors upon reasonable request. Source data are provided with this paper.

References

49. Ye, F., Liu, Y., Whitfield, R., Osborn, R. & Rosenkranz, S. Implementation of cross correlation for energy discrimination on the time-of-flight spectrometer CORELLI. *J. Appl. Crystallogr.* **51**, 315–322 (2018).
50. Goodge, B. et al. Disentangling coexisting structural order through phase lock-in analysis of atomic-resolution STEM data. *Microsc. Microanalysis.* **28**, 404–411 (2022).
51. Blaha, P. et al. WIEN2k: an APW+lo program for calculating the properties of solids. *J. Chem. Phys.* **152**, 074101 (2020).
52. Perdew, J., Burke, K. & Ernzerhof, M. Generalized gradient approximation made simple. *Phys. Rev. Lett.* **77**, 3865–3868 (1996).
53. Liechtenstein, A., Anisimov, V. & Zaanen, J. Density-functional theory and strong interactions: orbital ordering in Mott-Hubbard insulators. *Phys. Rev. B* **52**, R5467–R5470 (1995).
54. Ylvisaker, E., Pickett, W. & Koepernik, K. Anisotropy and magnetism in the LSDA+*U* method. *Phys. Rev. B* **79**, 035103 (2009).
55. Kresse, G. & Hafner, J. Ab initio molecular dynamics for liquid metals. *Phys. Rev. B* **47**, 558–561 (1993).
56. Kresse, G. & Joubert, D. From ultrasoft pseudopotentials to the projector augmented-wave method. *Phys. Rev. B* **59**, 1758–1775 (1999).
57. Togo, A. & Tanaka, I. First principles phonon calculations in materials science. *Scr. Mater.* **108**, 1–5 (2015).

Acknowledgements

This work is supported by the STC Center for Integrated Quantum Materials, NSF grant no. DMR-1231319. Materials growth and simulations were supported by the National Science Foundation (Platform for the Accelerated Realization, Analysis, and Discovery of Interface Materials (PARADIM)) under cooperative agreement no. DMR-2039380. This work used resources of the Advanced Light Source, which is a US Department of Energy (DOE) Office of Science User Facility under contract no. DE-AC02-05CH11231. The ARPES work was partially funded by the US DOE, Office of Science, Office of Basic Energy Sciences, Materials Sciences and Engineering Division, under contract no. DE-AC02-05CH11231 (Ultrafast Materials Program KC2203). Electron microscopy was carried out through the use of MIT.nano facilities at the Massachusetts Institute of Technology. Additional electron microscopy work was performed at Harvard University's Center for Nanoscale Systems, a member of the National Nanotechnology Coordinated Infrastructure Network, supported by the NSF under grant no. 2025158. A portion of this research used resources at the Spallation Neutron Source (SNS), a DOE Office of Science User Facility operated by the Oak Ridge National Laboratory (ORNL). ORNL is managed by UT-Battelle LLC for DOE's Office of Science, the single largest supporter of basic research in the physical sciences in the US. This manuscript has been authored by UT-Battelle LLC, under contract DE-AC05-00OR22725 with the US DOE. The US government retains and the publisher, by accepting the article for publication, acknowledges that the US government retains a non-exclusive, paid-up, irrevocable, worldwide license to publish or reproduce the published form of this manuscript, or allow others to do so, for US government purposes. DOE will provide public access to these results of federally sponsored research in accordance with the DOE Public Access Plan (http://energy.gov/downloads/doe-public-access-plan). Device fabrication work was performed at Harvard University's Center for Nanoscale Systems (CNS), a member of the National Nanotechnology Coordinated Infrastructure Network (NNCI), supported by the National Science Foundation under NSF grant no. 1541959. Any mention of commercial products within this paper is for information only; it does not imply recommendation or endorsement by NIST. Work at the NCNR was supported by the Department of Commerce. W.D.R. acknowledges support from the Department of Commerce. S.D. acknowledges support from the NSF Graduate Research Fellowship grant no. DGE-1745303. G.A.P. acknowledges support from the Paul & Daisy Soros Fellowship for New Americans and from the NSF Graduate Research Fellowship grant no. DGE-1745303. H.E.-S. and I.E.B. were supported by The Rowland Institute at Harvard. J.N. acknowledges support from the Swiss National Science Foundation under project no. P2EZP2_195686. C.T. acknowledges support from the Swiss National Science Foundation under project no. P2EZP2_191801. S.-Y.X. and C.T. were supported by NSF Career (Harvard fund 129522) DMR-2143177. H.L. and A.S.B. acknowledge support from NSF grant no. DMR-2045826 and the ASU Research Computing Center for the high-performance computing resources. J.A.M. acknowledges support from the Packard Foundation and Gordon and Betty Moore Foundation's EPiQS Initiative (grant GBMF6760).

Author contributions

Q.S., G.A.P., C.M.B. and J.A.M. synthesized the thin films with assistance from H.P. Q.S. and L.M. performed the ARPES measurements with support from A.S.B., C.J., E.R., D.F.S., Z.H. and A.L. S.D., Q.S. and J.A.M. performed the electrical measurements with assistance from J.T.H. H.E.-S. and I.E. characterized the samples with scanning transmission electron microscopy. G.A.P., S.D., J.R.E., D.F.S., Q.S., D.C.C., A.T.N. and P.S. performed the X-ray spectroscopy and scattering measurements. C.A.H., Y.L. and W.D.R. performed the neutron diffraction measurements. J.N., C.T. and S.-Y.X. performed the second-harmonic generation measurements. B.P. and A.S.B. performed the DFT calculations. J.A.M. conceived and guided the study. Q.S., S.D., L.M. and J.A.M. wrote the manuscript with discussion and contributions from all authors.

Competing interests

The authors declare no competing interests.

Additional information

Supplementary information The online version contains supplementary material available at https://doi.org/10.1038/s41567-022-01907-2.

Correspondence and requests for materials should be addressed to Luca Moreschini or Julia A. Mundy.

Peer review information *Nature Physics* thanks Jose Luis Garcia-Muñoz and the other, anonymous, reviewer(s) for their contribution to the peer review of this work.